RSC Advances

PAPER

View Article Online
View Journal | View Issue

Cite this: *RSC Adv.*, 2026, **16**, 12960

Multiresonant silicon-based nanopillar metasurface for narrowband RGB color filter

Zhengquan Jiang *

Received 4th January 2026
Accepted 4th March 2026

DOI: 10.1039/d6ra00072j

rsc.li/rsc-advances

The performance of conventional silicon (Si) -based metasurfaces is limited by intrinsic losses and low quality factors (*Q*). Here, we numerically investigate a silicon-based nanopillar RGB metasurface that exploits symmetry-tuned high-*Q* resonances (*Q*-BIC-like) enabled by intentional in-plane symmetry breaking. To mitigate substrate-induced non-radiative losses, a thin silicon nitride (Si_3N_4) interlayer is introduced between the metasurface and the Si substrate, providing improved refractive-index matching and reduced energy leakage into the substrate. This combined design leads to enhanced electromagnetic field confinement and narrower spectral responses. As a result, the reflection peak full width at half maximum (FWHM) is reduced from 103 nm and 77 nm to 51 nm and 48 nm for the red and green channels, respectively, accompanied by a 1.4× enhancement in local field intensity for the red channel. Furthermore, macro-pixel configurations based on Bayer-like arrangements demonstrate low spectral crosstalk and high color purity. These results demonstrate a practical metasurface design strategy for narrowband RGB color filtering in integrated micro-display and imaging applications.

1. Introduction

Metasurface-based spectral filtering technologies provide a promising route toward the development of highly miniaturized and densely integrated optical devices for applications such as high-resolution CMOS image sensors,[1] ultra-high-definition micro-displays,[2] hyperspectral imaging systems,[3] and compact spectrometers.[4] Unlike conventional optical filters that rely on material absorption to selectively attenuate specific wavelengths, metasurface spectral filters generate structural color through resonant coupling between incident light and subwavelength nanostructures patterned on the surface. As a result, metasurface-based filters offer several distinct advantages, including subwavelength spatial resolution, ultra-compact device footprints, excellent environmental stability, and full compatibility with standard CMOS fabrication processes. These features make metasurface spectral filters particularly attractive for next-generation integrated optoelectronic systems.

To date, the majority of metasurface filter designs have relied on plasmonic structures composed of noble metals such as gold and silver.[5–11] Although these structures exhibit strong local electric field confinement arising from surface plasmon resonances, their practical implementation is hindered by the high cost of noble metals, significant ohmic losses, and limited compatibility with CMOS manufacturing processes. These drawbacks restrict the scalability and long-term viability of plasmonic metasurface filters for large-area and high-density integration.

Dielectric metasurfaces based on silicon (Si) have therefore attracted increasing attention as an alternative platform for visible-wavelength applications. Si offers a high refractive index, comparatively low intrinsic optical losses relative to metallic structures, and excellent compatibility with mature CMOS fabrication technologies.[12–14] Si nanostructures can support a rich set of electric and magnetic Mie-type resonances,[15–17] enabling diverse functionalities such as perfect electromagnetic mirrors[18] and optical holography.[19] However, despite these advantages, the performance of Si metasurface is often severely limited by substrate-induced effects. As demonstrated by Dong *et al.*,[20] Si nanostructures integrated on solid substrates suffer substantial non-radiative energy leakage into the substrate, resulting in significantly reduced quality factors (*Q*) compared to their free-standing counterparts. Since the *Q*-factor directly influences the spectral linewidth, color saturation, and inter-channel crosstalk, substrate-induced losses pose a major obstacle to the deployment of Si metasurfaces in high-resolution display and imaging applications. To address the issue of low *Q*, the concept of quasi-bound states in the continuum (*Q*-BIC) has emerged as a powerful solution. For instance, Tian *et al.* demonstrated high-resolution tunable optical filters at telecommunication wavelengths using phase-change material-based BIC metasurfaces.[21] Inspired by such advances, applying BIC physics to CMOS-compatible silicon platforms offers a pathway to achieve narrowband filtering in the visible spectrum.

School of Microelectronics, Southern University of Science and Technology, Shenzhen 518055, China. E-mail: 12313506@mail.sustech.edu.cn

In this study, we present a design strategy for a silicon-based metasurface that suppresses radiative losses through symmetry-tuned high-Q resonances. Given that these modes are activated by symmetry breaking but are practically limited by material absorption, we refer to them as "Q-BIC-like" resonances throughout this work, while mitigating substrate-induced non-radiative leakage. A silicon nitride (Si_3N_4) interlayer is introduced between the metasurface and the Si substrate to improve refractive-index matching and reduce energy coupling into the substrate, thereby approximating a quasi-free-space optical environment. To enable robust excitation of Q-BIC-like modes and enhance electromagnetic field confinement, elliptical nanopillars are employed to deliberately break in-plane symmetry. Furthermore, two types of macro-pixel units are incorporated to evaluate pixel-level integration effects. Our numerical results show that even at high pixel densities, spectral crosstalk between macro-pixel units remains negligible, highlighting the potential of the proposed metasurface architecture for high-density RGB filtering in advanced imaging and micro-display technologies.

2. Metasurface design and simulation methodology

2.1 Suppression of non-radiative losses

A thin Si_3N_4 interlayer is selected based on an index-of-refraction matching guideline, in which the refractive index of the intermediate layer is chosen to match that of the surrounding media. Following the relation $n = n_1 \times n_2$, where $n_1 \approx 1$ represents the refractive index of the free-space environment (air) and $n_2 \approx 4$ corresponds to that of the Si substrate, the refractive index of Si_3N_4 ($n \approx 2$) satisfies this requirement, providing a more free-space-like optical environment at the metasurface–substrate interface.[20] This index-matching condition effectively mitigates substrate-induced non-radiative losses arising from resonant coupling into the Si substrate. Based on this structural configuration, finite-difference time-domain (FDTD) simulations are performed to systematically sweep the nanopillar diameter D and lattice period G. These numerical simulations are conducted using lumerical FDTD software with a mesh accuracy of 2. Periodic boundary conditions (PBC) are applied in the x- and y-directions to simulate the periodic array (the schematic of the periodic arrangement is shown in Fig. S4), while perfectly matched layer (PML) conditions are used in the z-direction to ensure efficient wave absorption. A custom index-of-merit function (IF) is employed to identify the optimal geometries for RGB filtering. The IF is defined as

$$\mathrm{IF} = \sum_{i=1}^{n} w_i \times \left| X_i - X_i^* \right|$$

where $n = 3$, and X_1, X_2, and X_3 correspond to the target resonance wavelength, peak reflectance, and FWHM, respectively. The weighting factors w_i are used to balance the relative importance of each parameter. The optimized geometric parameters obtained from this procedure are: red ($D = 160$, $G = 115$, $h_1 = 230$), green ($D = 120$, $G = 110$, $h_1 = 170$), blue ($D = 65$, $G = 60$, $h_1 = 115$). The corresponding simulated reflection spectra in Fig. 1b–d show that the red channel exhibits a peak reflectance of 0.81 at 682 nm with a FWHM of 103 nm, while the green channel reaches a peak reflectance of 0.76 at 561 nm with a FWHM of 77 nm. In contrast, the blue channel displays a lower peak reflectance of 0.31 at 419 nm with a FWHM of 44 nm. The reduced performance in the blue spectral region is attributed to the strong intrinsic optical absorption of Si at short wavelengths. The corresponding electric-field intensity distributions at the resonance wavelengths are presented in Fig. 2.

Fig. 2(a–c) present the electric-field intensity distributions of the red, green, and blue channels at their respective resonance wavelengths. The cross-sectional views in Fig. 2(d–f) clearly show that the Si_3N_4 interlayer enhances optical field confinement within the Si nanopillars by reducing electromagnetic coupling into the substrate, thereby mitigating substrate-induced non-radiative losses. At resonance, the multipolar decomposition (see Fig. S1 in SI) reveals that the reflection peaks are primarily driven by the excitation of a strong magnetic dipole (MD) mode. While the electric dipole (ED) and higher-order multipoles are also present, the MD resonance dominates the scattering behavior. This localized magnetic resonance leads to enhanced backward scattering, resulting in the observed reflection peaks.[22]

However, the reflection spectra in Fig. 1b–d exhibit relatively large linewidths, with FWHMs of 103 nm (red), 77 nm (green), and 44 nm (blue). This broadband spectral response arises because the resonance is primarily governed by a strong MD mode that exhibits significant radiative damping. As a result, the scattering profile of this dominant Mie mode spans a wide spectral range, leading to broadened resonance features. When the RGB channels are combined, this broad linewidth degrades color purity and increases inter-channel crosstalk. This limitation originates from the fact that conventional Mie resonances behave as bright modes that are strongly coupled to free space, resulting in substantial radiative losses and intrinsically low quality factors.

To overcome this limitation, we adopt an alternative design strategy that replaces conventional isotropic circular nanopillars with elliptically shaped nanopillars. The resulting in-plane symmetry breaking enables the excitation of Q-BIC-like with enhanced Q. By confining each color channel to its corresponding Q-BIC-like mode, radiative losses are effectively reduced, leading to narrower spectral linewidths, improved color purity, and reduced inter-channel crosstalk.

2.2. Reduction of radiative losses *via* Q-BIC-like excitation

Fig. 3a illustrates the unit-cell geometry after the introduction of in-plane symmetry breaking. By transforming the circular Si nanopillars into elliptical ones, the rotational symmetry of the structure is reduced from C_{4v}(possessing vertical mirror symmetries) to C_{1v}. This symmetry reduction disrupts the complete destructive interference of near-field dipole moments and induces a finite net dipole moment, thereby converting an originally symmetry-protected dark mode into a Q-BIC-like

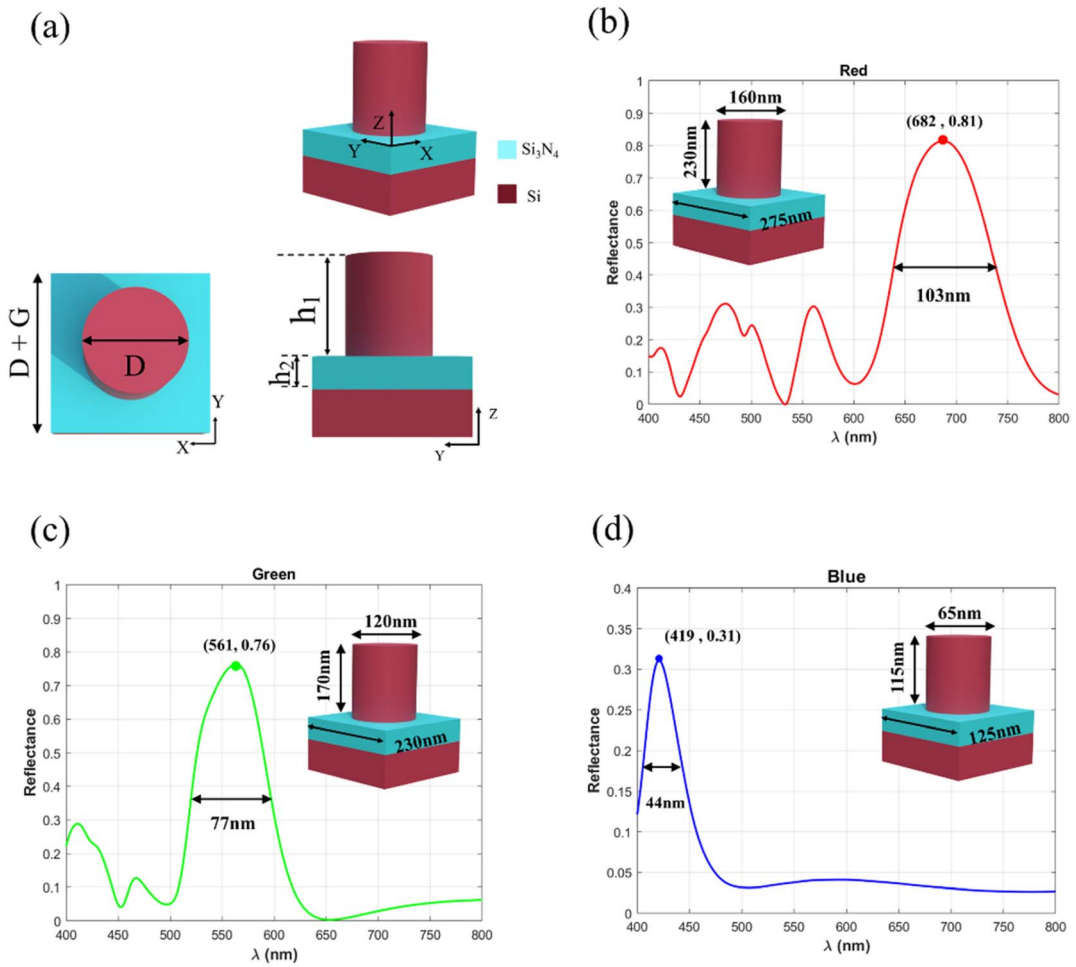

Fig. 1 Low-leakage metasurface design and simulated RGB reflection spectra. (a) Schematic of the metasurface unit cell, where a thin 70 nm Si_3N_4 interlayer is inserted between the Si nanopillars and the Si substrate to mitigate substrate-induced energy leakage arising from resonant coupling into the substrate. (b–d) Simulated reflection spectra of isotropic circular nanopillar metasurface for the red, green, and blue channels, respectively. The peak wavelengths, peak reflectance values, and corresponding full width at half maximum (FWHM) are indicated in each spectrum.

mode. The symmetry-protected nature of this BIC arises from the mismatch between the spatial symmetry of the localized mode and the external radiation continuum at the Γ-point, which is subsequently accessed by reducing the unit-cell symmetry from C_{4v} to C_{1v}[23] (see details in Fig. S2 and S3). In the proposed design, the short-axis length d and the rotation angle θ are introduced as additional geometric parameters, with θ fixed at 45° and 135°. The same parameter-scanning and optimization strategy employed for the circular nanopillars is applied here, whereby the parameters D, G, and d are systematically swept and optimal geometries are selected using the IF.

The optimized geometrical parameters are obtained as follows: red ($D = 190$ nm, $G = 130$ nm, $h_1 = 230$ nm, $d = 129$ nm), green ($D = 150$ nm, $G = 100$ nm, $h_1 = 170$ nm, $d = 102$ nm) and blue ($D = 65$ nm, $G = 60$ nm, h_1; $= 115$ nm, $d = 66$ nm). The corresponding simulated reflection spectra in Fig. 3b clearly demonstrate the advantages of Q-BIC-like excitation. Specifically, the FWHM of the red channel is reduced from 103 nm to 51 nm, corresponding to a linewidth narrowing of over 50%, while the green channel exhibits a reduction from 77 nm to 48 nm, representing nearly a 40% improvement. In contrast, the linewidth reduction in the blue spectral region is considerably less pronounced. This behavior is attributed to the intrinsically high optical absorption of Si at shorter wavelengths, where material absorption rather than radiative loss dominates the overall Q-factor, thereby limiting the effectiveness of geometric tuning for Q enhancement in the blue band. Furthermore, to evaluate the practical applicability of the proposed design in real-world optical systems, such as those involving high-NA focusing, we investigated the angular robustness of the metasurfaces. The evolution of the reflection spectra as a function of the incident angle is illustrated in Fig. S5 (see details in SI). The results demonstrate that the resonance peak remains substantially stable for incident angles up to 20°, confirming the robust performance of our design within a practical angular range suitable for conventional imaging and display technologies.

Fig. 3c presents the top-view and cross-sectional electric-field intensity distributions at the resonance wavelengths of the

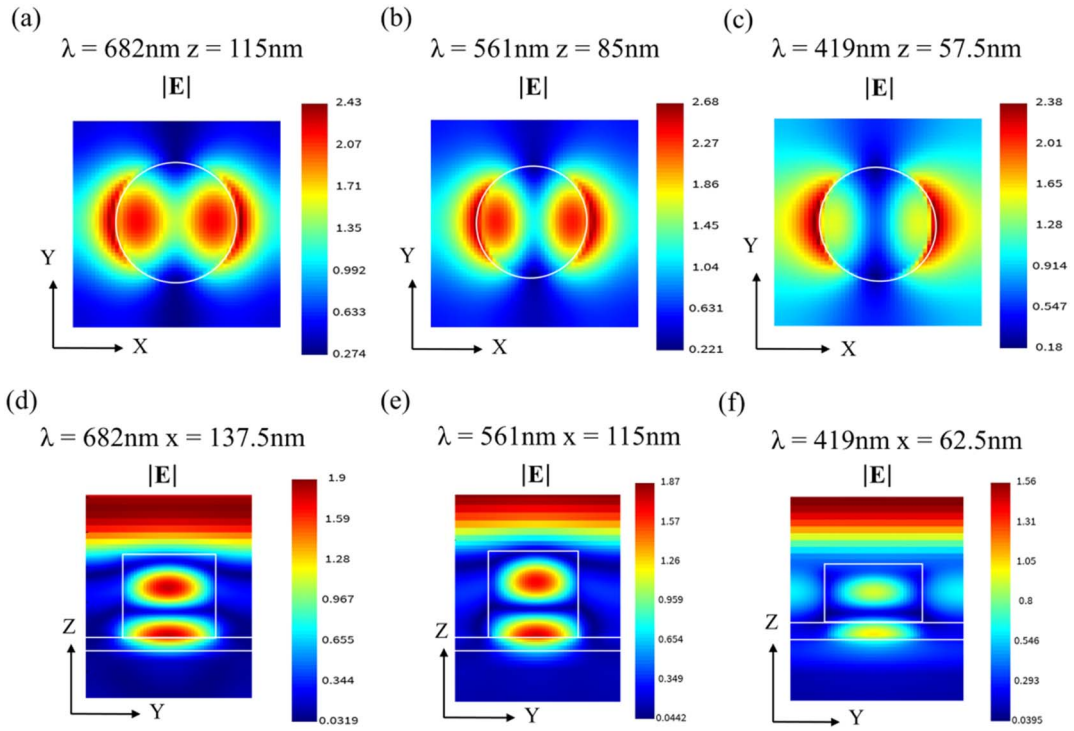

Fig. 2 Electric-field intensity distributions at the resonance wavelengths. (a–c) Top-view and (d–f) cross-sectional electric-field distributions corresponding to the red, green, and blue circular nanopillar metasurface, respectively.

elliptical nanopillar metasurfaces. To evaluate the influence of the *Q*-BIC-like mechanism on electromagnetic field confinement, these results are directly compared with the corresponding field distributions of circular nanopillars shown in Fig. 2. For the circular structures, although pronounced standing-wave patterns are observed above the nanopillars, the internal field intensity within the Si remains relatively weak, indicating inefficient photon confinement associated with conventional Mie-type resonances. In this case, a significant portion of the electromagnetic energy rapidly radiates back into free space, resulting in low *Q*.

In contrast, the elliptical nanopillar structures exhibit a markedly enhanced degree of optical field confinement. While the standing-wave intensity above the pillars is slightly reduced—consistent with longer photon lifetimes and increased interaction with the absorbing Si material—the internal electric-field intensity within the nanopillars is substantially increased. Quantitative evaluation of the local electric-field intensity $|E|^2$ in the vicinity of the nanopillars reveals that *Q*-BIC-like excitation effectively reduces radiative losses, leading to a significant accumulation of electromagnetic energy within the resonator. In particular, the internal field intensity of the red-channel elliptical nanopillar is approximately 1.4× higher than that of the corresponding circular structure. The enhancement observed for the green and blue channels is comparatively weaker due to the intrinsically higher optical absorption of Si at shorter wavelengths, where material absorption increasingly dominates the total loss budget.

The cross-sectional field profiles further demonstrate strong localization of electromagnetic energy within the Si nanopillars and at the Si–Si_3N_4 interface, a characteristic feature of *Q*-BIC-like modes that exhibit minimal external radiation and pronounced internal confinement within subwavelength resonant cavities. Examination of the top-view field maps reveals that the maximum field concentration occurs near the two ends of the major axis of the elliptical nanopillars, providing direct evidence of the modal asymmetry introduced by in-plane symmetry breaking.

Taken together, the pronounced linewidth narrowing observed in Fig. 3b–d is in direct correspondence with the enhanced internal field confinement shown in Fig. 3c, confirming that the excitation of *Q*-BIC-like modes simultaneously suppresses radiative losses in the spectral domain and localizes electromagnetic energy in the spatial domain.

2.3. Integrated macro-pixel architectures and crosstalk analysis

To evaluate the feasibility of the proposed metasurface design for practical high-density display and imaging applications, two representative macro-pixel configurations were constructed from the optimized unit-cell designs, and their ability to suppress color crosstalk was systematically investigated. The first macro-pixel configuration adopts a 2 × 2 Bayer-like arrangement. As illustrated in Fig. 4a, the proposed design incorporates two blue sub-pixels rather than the four sub-pixels used in the conventional RGGB Bayer pattern commonly employed in commercial display technologies. This

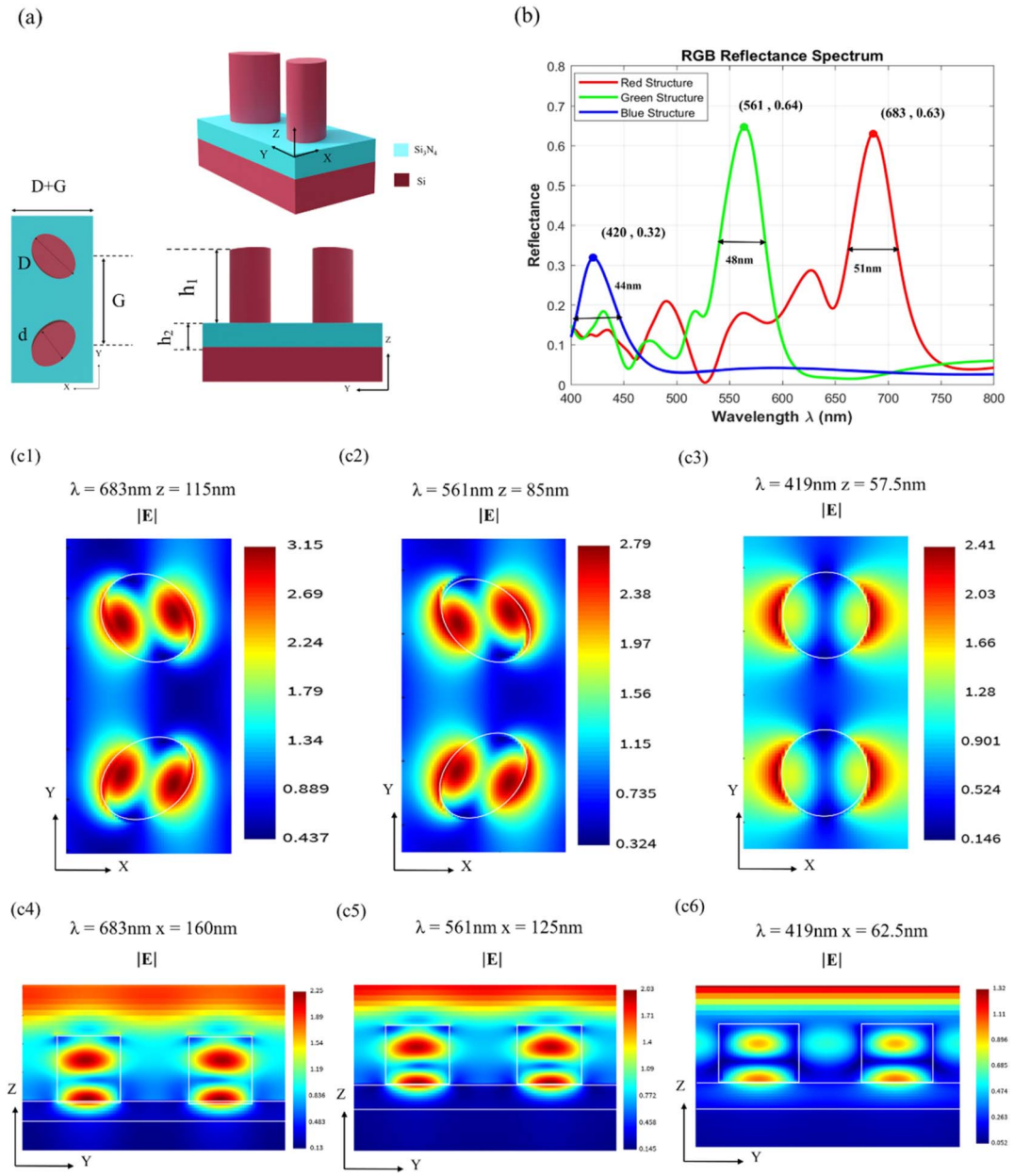

Fig. 3 Suppression of radiative losses using *Q*-BIC-like enabled metasurface structures. (a) Schematic of the unit cell, in which isotropic circular nanopillars are replaced by elliptical nanopillars to introduce in-plane symmetry breaking and enable excitation of *Q*-BIC-like. (b) Simulated reflection spectra of the red, green, and blue channels, with peak wavelengths, peak reflectance values, and corresponding FWHM indicated. (c1–c3) Top-view and (c4–c6) cross-sectional electric-field intensity distributions of the elliptical nanopillar metasurface at their respective resonance wavelengths.

modification increases the effective blue-reflective area, compensating for the intrinsically lower reflectivity of Si in the blue spectral region and resulting in improved intensity matching among the RGB channels. After balancing the trade-offs between sub-pixel count and overall device footprint, the macro-pixel dimensions were set to 9 μm × 9 μm, with each RGB sub-pixel occupying an area of 4.5 μm × 4.5 μm. The second macro-pixel configuration, shown in Fig. 4c, employs a linear RGB stripe arrangement. In this design, each color channel is assigned a distinct spatial periodicity based on the optimized parameters of the corresponding unit pixel. Specifically, the red sub-pixel has dimensions of 6.50 μm × 6.40 μm, while the green and blue sub-pixels both measure 6.50 μm × 6.50 μm. Consequently, the total macro-pixel size is 6.5 μm × 19.4 μm (6.5 + 6.5 + 6.4 μm). The numerical investigation of these macro-pixel configurations was performed using the finite-difference time-domain (FDTD) method (Lumerical). To simulate the spectral response, PML boundary conditions were applied in all directions (x, y, and z). A reflection monitor was positioned above the structure to collect the total reflected

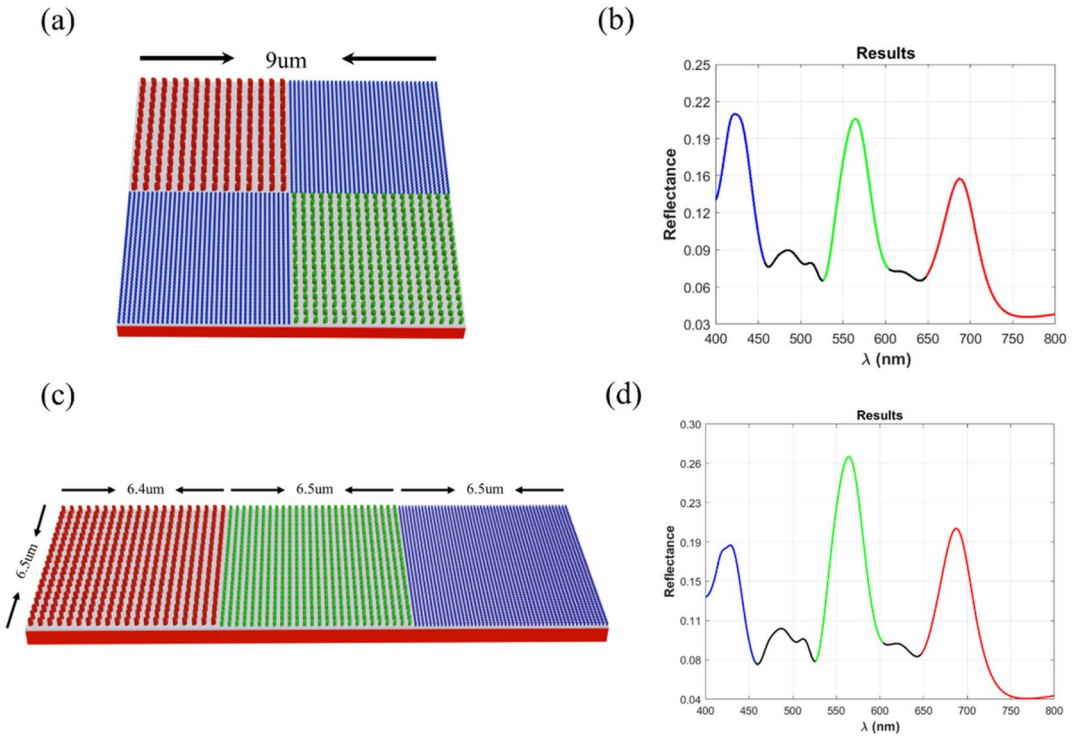

Fig. 4 Schematic illustrations of two integrated macro-pixel configurations and their corresponding simulated reflection spectra. (a) Bayer-like macro-pixel configuration. (c) RGB linear stripe (R–G–B) macro-pixel configuration. (b and d) Simulated reflection spectra corresponding to the Bayer-like and stripe configurations, respectively. Red, green, and blue curves represent the responses of the three color channels, while black curves indicate the spectral responses arising from adjacent sub-pixels, used to evaluate inter-channel crosstalk.

power. A conformal mesh with a minimum mesh size of 2 nm was used.

Fig. 4b–d present the simulated reflection spectra for the two macro-pixel configurations. The red, green, and blue curves correspond to the respective RGB channels, while the black curves represent the spectral response of neighboring sub-pixels when observed from an adjacent color channel, providing a quantitative assessment of inter-pixel crosstalk. For comparison, Fig. 3b shows the spectra of isolated unit pixels. When integrated into macro-pixel configurations, the reflection spectra exhibit a proportional reduction in peak reflectance relative to the isolated unit-pixel response. This reduction arises from area-fraction effects, as the total reflected power is normalized over the macro-pixel area, while only one-quarter of the area is occupied by each RGB channel in the Bayer-like configuration or one-third in the stripe configuration. Accordingly, the reduced peak intensities of the macro-pixel spectra closely correspond to the respective area fractions of each color channel. Despite the reduction in overall reflectance, both macro-pixel configurations maintain clearly separated RGB spectral peaks. The spectral line shapes of the individual color channels exhibit no significant distortion, and the resonant wavelengths remain stable at approximately 420 nm for blue, 560 nm for green, and 690 nm for red. These results indicate that the proposed metasurface architecture preserves strong spectral separation even under dense spatial integration. The supported *Q*-BIC-like modes confine electromagnetic energy within each Si nanopillar, thereby limiting energy leakage and reducing coupling between adjacent color channels. As a result, very low levels of spectral crosstalk are achieved, even when the pixels are tightly packed.

Overall, these simulation results demonstrate that the proposed metasurface design holds strong potential for the development of micron-scale, high-quality display technologies, densely integrated on-chip sensor arrays, and other optical systems requiring high color purity within stringent spatial constraints.

3. Conclusion

In this work, we numerically investigated an silicon-based nanopillar metasurface for narrowband RGB color filtering. By introducing in-plane symmetry breaking, *Q*-BIC-like was exploited to effectively reduce radiative losses, resulting in enhanced electromagnetic field confinement and narrowed spectral linewidths. In addition, a thin Si_3N_4 interlayer was incorporated to mitigate substrate-induced energy leakage through improved refractive-index matching. As a result, the reflection linewidths of the red and green channels were reduced to 51 nm and 48 nm, respectively, accompanied by improved color selectivity. Furthermore, macro-pixel configurations based on Bayer-like and stripe arrangements were evaluated to assess pixel-level integration effects. The simulation results show that the proposed metasurface design

maintains well-separated RGB responses with low spectral crosstalk even under dense spatial integration. While the performance in the blue spectral region remains limited by the intrinsic optical absorption of Si, the overall results demonstrate a feasible and practical metasurface design strategy for compact RGB color filtering. This approach is well suited for integrated display and imaging systems where narrow spectral responses, low crosstalk, and CMOS compatibility are required. Although our work focuses on a reflection-mode design for specific applications such as reflective displays and anti-counterfeiting, we acknowledge that transmission-mode filters are more commonly used in other contexts like image sensors. Future studies could explore adapting our design for transmission by using a transparent substrate or backside illumination. The benefits from current structure are still the good Q factor and design simplicity.

Conflicts of interest

There are no conflicts to declare.

Data availability

The data that support the findings of this study are available from the corresponding author upon reasonable request.

Supplementary information (SI): this document includes Fig. S1 (multipolar decomposition of circular and elliptical nanopillars), Fig. S2 (Q-factor analysis *versus* symmetry parameters), Fig. S3 (spectral evolution maps), Fig. S4 (array layout schematic), and Fig. S5 (angular dependence of reflection spectra). See DOI: https://doi.org/10.1039/d6ra00072j.

References

1 X. Zou, *et al.*, Pixel-level Bayer-type colour router based on metasurfaces, *Nat. Commun.*, 2022, **13**(1), 3288.
2 W. J. Joo, *et al.*, Metasurface-driven OLED displays beyond 10,000 pixels per inch, *Science*, 2020, **370**(6515), 459–463.
3 M. Faraji-Dana, E. Arbabi, A. Arbabi, S. M. Kamali, H. Kwon and A. Faraon, Compact folded metasurface spectrometer, *Nat. Commun.*, 2018, **9**(1), 4196.
4 A. Tittl, *et al.*, Imaging-based molecular barcoding with pixelated dielectric metasurfaces, *Science*, 2018, **360**(6393), 1105–1109.
5 K. Kumar, H. Duan, R. S. Hegde, S. C. W. Koh, J. N. Wei and J. K. W. Yang, Printing colour at the optical diffraction limit, *Nat. Nanotechnol.*, 2012, **7**(9), 557–561.
6 S. J. Tan, *et al.*, Plasmonic color palettes for photorealistic printing with aluminum nanostructures, *Nano Lett.*, 2014, **14**(7), 4023–4029.
7 X. M. Goh, *et al.*, Three-dimensional plasmonic stereoscopic prints in full colour, *Nat. Commun.*, 2014, **5**, 5361.
8 J. S. Clausen, *et al.*, Plasmonic metasurfaces for coloration of plastic consumer products, *Nano Lett.*, 2014, **14**(8), 4499–4504.
9 A. Kristensen, *et al.*, Plasmonic colour generation, *Nat. Rev. Mater.*, 2016, **2**, 16088.
10 X. Duan, S. Kamin and N. Liu, Dynamic plasmonic colour display, *Nat. Commun.*, 2017, **8**, 14606.
11 Y. Chen, *et al.*, Hydrogen-regulated chiral nanoplasmonics, *Nano Lett.*, 2017, **17**(9), 5555–5560.
12 A. I. Kuznetsov, A. E. Miroshnichenko, Y. H. Fu, J. Zhang and B. Luk'yanchuk, Magnetic light, *Sci. Rep.*, 2012, **2**, 492.
13 A. I. Kuznetsov, A. E. Miroshnichenko, M. L. Brongersma, Y. S. Kivshar and B. Luk'yanchuk, Optically resonant dielectric nanostructures, *Science*, 2016, **354**(6314), aag2472.
14 A. B. Evlyukhin, *et al.*, Demonstration of magnetic dipole resonances of dielectric nanospheres in the visible region, *Nano Lett.*, 2012, **12**(7), 3749–3755.
15 Y. F. Yu, A. Y. Zhu, R. Paniagua-Domínguez, Y. H. Fu, B. Luk'yanchuk and A. I. Kuznetsov, High-transmission dielectric metasurface with 2 phase control at visible wavelengths, *Laser Photon. Rev.*, 2015, **9**(4), 412–418.
16 Y. Yang, W. Wang, P. Moitra, I. I. Kravchenko, D. P. Briggs and J. Valentine, Dielectric meta-reflectarray for broadband high-efficiency optical vortex generation, *Nano Lett.*, 2014, **14**(3), 1394–1399.
17 U. Levy, M. Abashin, K. Ikeda, A. Krishnamoorthy, J. Cunningham and Y. Fainman, Inhomogeneous dielectric metamaterials with space-variant polarizability, *Phys. Rev. Lett.*, 2007, **98**(24), 243901.
18 R. Paniagua-Domínguez, *et al.*, Generalized Brewster effect in dielectric metasurfaces, *Nat. Commun.*, 2016, **7**, 10362.
19 B. Wang, *et al.*, Visible-frequency dielectric metasurfaces for multi-dimensional light manipulation, *Nano Lett.*, 2016, **16**(8), 5235–5240.
20 Z. Dong, J. Ho, Y. F. Yu, Y. H. Fu, R. Paniagua-Dominguez, S. Wang, A. I. Kuznetsov and J. K. W. Yang, Printing Beyond sRGB Color Gamut by Mimicking Silicon Nanostructures in Free-Space, *Nano Lett.*, 2017, **17**(12), 7620–7628.
21 F. Tian, J. Zhou, E. Abraham and Z. Liu, Tunable dielectric BIC metasurface for high resolution optical filters, *J. Phys. D: Appl. Phys.*, 2023, **56**(13), 134002, DOI: 10.1088/1361-6463/acb55d.
22 M. Kerker, D. S. Wang and C. L. Giles, Electromagnetic scattering by magnetic spheres, *J. Opt. Soc. Am.*, 1983, **73**(6), 765–767.
23 Y. G. Ki, H. W. Jeon and S. J. Kim, Design of metasurface-based photodetector with high-quality factor, *Electronics*, 2024, **13**(4), 753, DOI: 10.3390/electronics13040753.